

U.S. DEPARTMENT OF COMMERCE
National Technical Information Service

AD-A024 550

AN INVESTIGATION OF MECHANISMS OF INITIATION OF
LASER-SUPPORTED ABSORPTION (LSA) WAVES

BATTELLE COLUMBUS LABORATORIES

PREPARED FOR
ARMY MISSILE COMMAND

JANUARY 1975

Best possible scan

REPRODUCED BY
NATIONAL TECHNICAL
INFORMATION SERVICE
U. S. DEPARTMENT OF COMMERCE
SPRINGFIELD, VA. 22161

Best possible scan



REPORT DOCUMENTATION PAGE		READ INSTRUCTIONS BEFORE COMPLETING FORM
1. REPORT NUMBER	2. GOVT ACCESSION NO.	3. RECIPIENT'S CATALOG NUMBER
4. TITLE (and Subtitle) An Investigation of Mechanisms of Initiation of Laser-Supported Absorption (LSA) Waves ✓		5. TYPE OF REPORT & PERIOD COVERED Semiannual July 15, 1974-January 15, 1975 ✓
7. AUTHOR(s) C. T. Walters, R. H. Barnes, and R. E. Beverly		8. CONTRACT OR GRANT NUMBER(s) DAAH01-74-C-0776 ✓
9. PERFORMING ORGANIZATION NAME AND ADDRESS Battelle Columbus Laboratories ✓ 505 King Avenue, Columbus, Ohio 43201		10. PROGRAM ELEMENT, PROJECT, TASK AREA & WORK UNIT NUMBERS 62301E, ARPA-A02113, 2E20, 003D1
11. CONTROLLING OFFICE NAME AND ADDRESS ARPA 1400 Wilson Boulevard Arlington, Virginia 22209		12. REPORT DATE January, 1975 ✓
14. MONITORING AGENCY NAME & ADDRESS (if different from Controlling Office) US Army Missile Command Redstone Arsenal, Alabama 35809 Attention AMSMI-RNS		13. NUMBER OF PAGES
		15. SECURITY CLASS (of this report) Unclassified
		15a. DECLASSIFICATION DOWNGRADING SCHEDULE
16. DISTRIBUTION STATEMENT (of this Report) Distribution of this document is unlimited		
17. DISTRIBUTION STATEMENT (of the abstract entered in Block 20, if different from Report)		
18. SUPPLEMENTARY NOTES		
19. KEY WORDS (Continue on reverse side if necessary and identify by block number) Laser-Supported Absorption Waves Surface Physics Laser-Supported Detonation Waves Plasma Diagnostics Plasma Production Thermionic Emission Self-Shielding TEA CO ₂ Laser Effects Laser Interaction with Materials		
20. ABSTRACT (Continue on reverse side if necessary and identify by block number) Additional experimental results of a study of LSD-wave initiation processes are reported. The first measurements of delay time to initiation on nonmetallic materials are presented. In metallic studies, target emission of electrons from aluminum 2024, lead, and tungsten surfaces were recorded at atmospheric pressure prior to LSD-wave initiation. No surface damage was observed on the tungsten surface at 2000X in SEM inspections after irradiation, while lead and aluminum exhibited defect-oriented damage. Time-resolved spectroscopy experiments with aluminum 2024 revealed a dramatic drop in the ionized aluminum vapor emissions (Continued)		

20. ABSTRACT (Continued)

above the air pressure threshold for LSD-wave initiation (5-10 torr at 3.2×10^8 watt/cm²).

TABLE OF CONTENTS

	<u>Page</u>
INTRODUCTION	4
RESEARCH DETAILS	5
CONCLUSIONS.	45
FUTURE EFFORT.	46
REFERENCES	47

LIST OF FIGURES

Figure 1. Initiation Timing Probe Assembly	6
Figure 2. Initiation Timing Probe Response	7
Figure 3. SEM Records Before and After One Pulse at Atmospheric Pressure (2000X)	10
Figure 4. Variation in Target Emission Records with Target Plane Location, $G_p = 2.14 \times 10^8$ watt/cm ²	15
Figure 5. Target Emission Records at Atmospheric Pressure $G_p = 3.2 \times 10^8$ watt/cm ²	16
Figure 6. Breakdown Times Inferred from Target Emission Records at Atmospheric Pressure.	18
Figure 7. Target Voltage at Breakdown for Atmospheric Pressure	20
Figure 8. Pressure Dependence of Target Voltage and Breakdown Time for Aluminum 2024 at 1.28×10^8 watt/cm ²	23
Figure 9. Neutral Aluminum Vapor Emissions at Low Air Pressures for 3.2×10^8 watt/cm ²	33
Figure 10. Ionized Aluminum Emission on the Target Surface at 3 μ sec ($G_p = 3.2 \times 10^8$ watt/cm ²	34
Figure 11. Total Emission at 3587.06 A (Al II) Above and Below Pressure Threshold for LSD-Wave Initiation, $G_p = 3.2 \times$ 10^8 watt/cm ²	35
Figure 12. Aluminum Target Spectra Near 3500 A.	37
Figure 13. Zinc Target Spectra Near 3500 A.	38
Figure 14. Tungsten Target Spectra Near 3500 A.	39

LIST OF FIGURES (Continued)

Figure 14.	Tungsten Target Spectra Near 3500 A.	39
Figure 15.	Lead Target Spectra Near 3500 A.	40
Figure 16.	Copper Target Spectra Near 3500 A.	41
Figure 17.	Titanium Target Spectra Near 3500 A (2.14×10^8 watt/cm ²).	42
Figure 18.	Graphite Target Spectra Near 3500 A (2.14×10^6 watt/cm ²).	43
Figure 19.	Type 304 Stainless Steel Target Near 3500 A (2.14×10^8 watt/cm ²).	44

LIST OF TABLES

Table 1.	Handbook Metal Property Data	9
Table 2.	Analysis of the Effects of Multiple Shots on Prompt Emission (Positive Bias Signal).	28
Table 3.	Comparison of Prompt Signals at $G_p = 2.14 \times 10^8$ watt/cm ²	29
Table 4.	Average Ion Expansion Energies.	30
Table 5.	Excited-State Energies of Transient Species Observed . . .	32

SUMMARY

This report presents results of additional experimental effort in the study of the initiation of laser-supported absorption (LSA) waves on solid surfaces irradiated in air with pulsed laser radiation. LSA waves may be classified as either supersonic, so-called laser-supported detonation (LSD) waves, or as subsonic, so-called laser-supported combustion (LSC) waves. In either case, a hot-air plasma (1-2 eV) is formed which propagates back up the laser beam away from the target surface and absorbs most of the laser-beam energy. The objective of this study is to provide an improved understanding of the process of LSA wave initiation. The experiments of the current contract deal exclusively with initiation of LSD waves; however, diagnostic techniques being developed and experimental results being obtained may be directly applicable to the LSC problem.

During the first year of study, experiments were directed toward understanding the mechanisms of initiation of LSD waves produced on practical aluminum surfaces in air with the Battelle 75-joule TEA CO₂ laser. Results indicated that the initiation occurred at a large number of local surface features (laminae and pits) on a very rapid time scale (30-60 nsec). Thermionic emission at these surface features was found to be a viable mechanism for initiation of the local LSD-wave plasmas. Initial studies of nonmetallic LSD-wave initiation showed that the initiation process is also local for "first shot" irradiations of acrylic plastic and fused silica.

During this report period initial data were taken on the delay time to initiation of LSD waves on nonmetallic materials. Measurements utilized a modified ring electrostatic probe to detect the photoionization of air at the time of initiation. For initial irradiations of acrylic plastic, breakdown times are similar to those for aluminum 2024 (\approx 30 nsec).

Scanning electron microscope and target electron emission data were recorded for aluminum 2024, tungsten, and lead samples irradiated at atmospheric pressure. Initiation behavior of lead was found to be very similar to that for aluminum 2024, while tungsten initiation delay times

were about 20 nsec longer. No damage was observed on the tungsten surface at 2000X. Measurements of target emission at reduced air pressure were performed for the aluminum 2024 samples. The increase in target voltage with decreasing pressure was faster than predicted by a simple one-dimensional diffusion-controlled model for the priming-electron spatial distribution.

Charge collection measurements were performed in hard vacuum in an attempt to determine the target-surface-emitted electron energy distribution prior to initiation. Large background probe signals, apparently arising from electrons photoemitted from the target surface after plasma initiation, rendered the results inconclusive.

Time-resolved emission spectroscopy measurements were performed for irradiations of aluminum 2024 samples at air pressures ranging from 10^{-6} torr to 1 atm. Six aluminum lines were studied, including emissions characteristic of both neutral and one-ionized species. Ionized aluminum vapor emissions at the target surface were found to peak near the pressure threshold for LSD-wave initiation (5-10 torr at 3.2×10^8 watt/cm²) and drop below the background bremsstrahlung level for pressures greater than 20 torr. Time-integrated spectra were recorded in the range 2250 to 6500 Å for several metals in air pressures ranging from 10^{-6} torr to 1 atm. These data have not yet been analyzed; however, typical spectra are presented.

ACKNOWLEDGEMENT

The authors wish to gratefully acknowledge the excellent technical assistance of Warren B. Nicholson in the laser irradiations and diagnostic instrumentation, Charles C. Moeller in the spectroscopy experiments, and Roy K. White in the scanning electron microscopy.

AN INVESTIGATION OF MECHANISMS OF INITIATION
OF LASER-SUPPORTED ABSORPTION (LSA) WAVES

by

C. T. Walters, R. H. Barnes, and R. E. Beverly III

INTRODUCTION

This is the third semiannual report of an experimental investigation of initiation of laser-supported absorption (LSA) waves in gases in front of solid surfaces. Current contract efforts are limited to experimental study of initiation of absorption waves generated by short pulses, i.e., laser-supported detonation (LSD) waves, however, results may be applicable to laser-supported combustion (LSC) waves in some cases. During the first year^{(1,2)*}, extensive studies of initiation of LSD waves in air in front of practical aluminum surfaces with TEA CO₂ laser pulses have revealed a viable mechanism of initiation. The experimental data are consistent with inverse-bremsstrahlung heating of surface-emitted priming electrons in the air. Thermionic or field emission at surface features such as pits and laminae is believed to be the process for production of priming electrons for the air breakdown. During the second year of research, the universality of this mechanism is being studied in experiments designed to reveal initiation mechanisms on a variety of metallic and nonmetallic materials. Metallic materials being studied include aluminum, titanium, tungsten, copper, stainless steel, lead, and certain metals having special surface preparations. Nonmetallic materials include acrylic plastic, fused silica, cellulose acetate, unfilled polymer coating, Pyroceram, potassium chloride, and silicon. In addition, pressure measurements are being performed in air and vacuum to assess the effects of the LSD/blast wave on metallic and nonmetallic target response to the TEA laser pulse. Of particular interest is the effect of time delay of LSD-wave initiation.

* References are listed on page 47.

RESEARCH DETAILS

Timing Probe Development

A key measurement in the assessment of LSD-wave initiation is the measurement of breakdown time, i.e., the time interval between the time at which laser radiation first arrives on the target surface and the time at which an absorbing plasma is observed. From research during the first year, it was found that the ultraviolet-radiation-induced precursor pulse on an electrostatic probe placed near the interaction region is a good indicator of breakdown time. Some effort during this research period was devoted to designing a timing probe based on this principle which would be compatible with nonconducting target material and other diagnostics. Initial efforts with an asymmetrically located probe revealed insufficient sensitivity and a new ring probe assembly was constructed. The new probe has sensitivity similar to that of the original electrostatic ring probe⁽¹⁾ but is comparable with, and attaches to, the target emission probe assembly and may be used with nonmetallic targets. Figure 1 shows schematically the target emission probe assembly with the new electrostatic ring probe attached. The probe itself is constructed of 0.102-cm-diameter copper wire bent into a ring having 1.35-cm inside diameter. The distance between the plane of the ring and the target surface is adjustable. The circuitry used for the probe is identical to that presented in Figure 10 of Reference (1).

Several irradiations were performed on aluminum 2024 at atmospheric pressure to confirm operation of the probe consistent with previous work. Figure 2(a) illustrates probe response for a positive bias of 20 volts and peak power density of 5.8×10^8 watt/cm². While the shape of the voltage trace is different from that shown in Reference (1), the essential features indicative of plasma initiation and blast-wave arrival remain. On the trace, the first rise of probe current results from photoionization of gas around the probe by ultraviolet emission from the LSD plasma. Shape and voltage

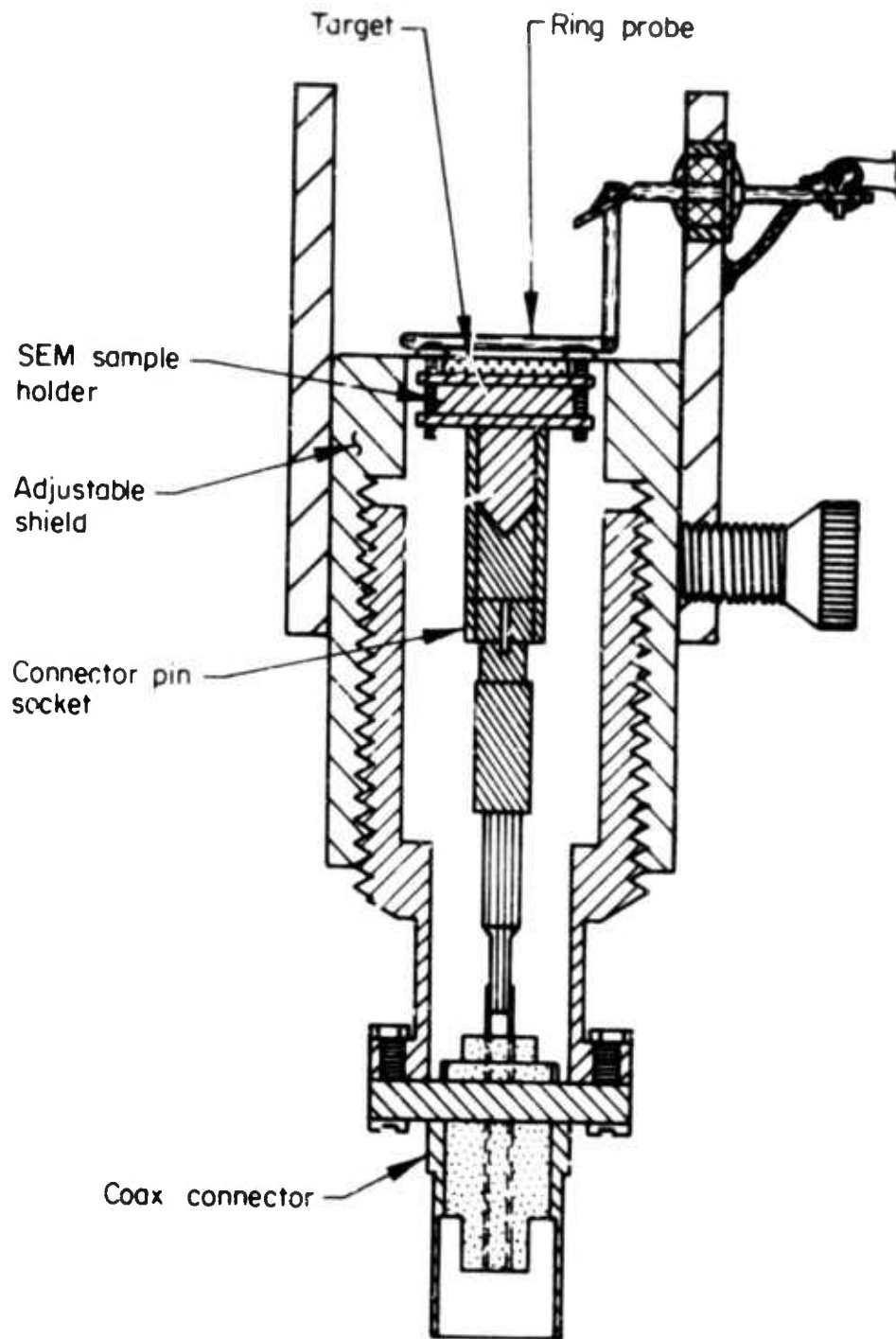
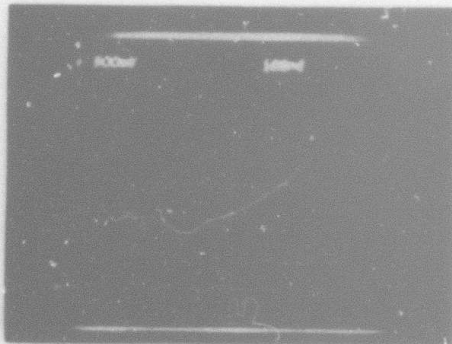
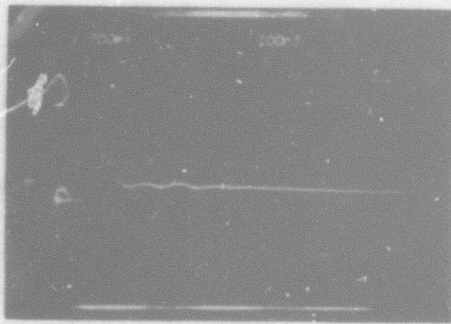


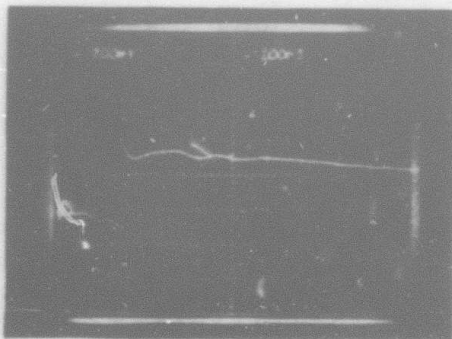
FIGURE 1. INITIATION TIMING PROBE ASSEMBLY



- (a) Aluminum 2024, $V_p = +20$ v, $G_p = 5.8 \times 10^8$ watt/cm²
 (500 mv/cm-inverted, 100 nsec/cm)



- (b) Acrylic Plastic (first shot), $V_p = +24$ v, $G_p = 3.5 \times 10^8$ watt/cm²
 (200 mv/cm-inverted, 100 nsec/cm)



- (c) Acrylic Plastic (second shot), $V_p = +24$ v, $G_p = 3.5 \times 10^8$ watt/cm²
 (200 mv/cm-inverted, 100 nsec/cm)

FIGURE 2. INITIATION TIMING PROBE RESPONSE

level differences result from differences in ring diameter and location. Measured initiation times of 25-30 nsec for 5.8×10^8 watt/cm² agreed quite well with previous aluminum 2024 data.

During this period the first initiation timing measurements were made for nonmetallic targets. Figure 2(b) and (c) present probe responses for the first and second shot on acrylic plastic at 3.5×10^8 watt/cm² peak power density with +24 volts probe bias. First appearance of probe current occurs 25-30 nsec into the laser pulse at this intensity for up to three pulses on the same surface. Blast-wave arrival times (not seen in the figure) were of order 1.8 μ sec. An interesting prompt bias effect is seen on the first-shot only (Figure 2(b)) which is not seen in the metallic results. If the first shot initiation involves thermionic emission of electrons from isolated metallic debris, as discussed in Reference (2), then the absence of a conducting target surface would result in higher space-charge-induced currents in the probe. This effect is absent or reduced in subsequent shots. Of particular interest will be probe response at lower intensities where a second shot does not initiate an LSD wave on acrylic plastic. During the latter part of the program, a complete series of initiation timing experiments will be performed for nonmetallic materials.

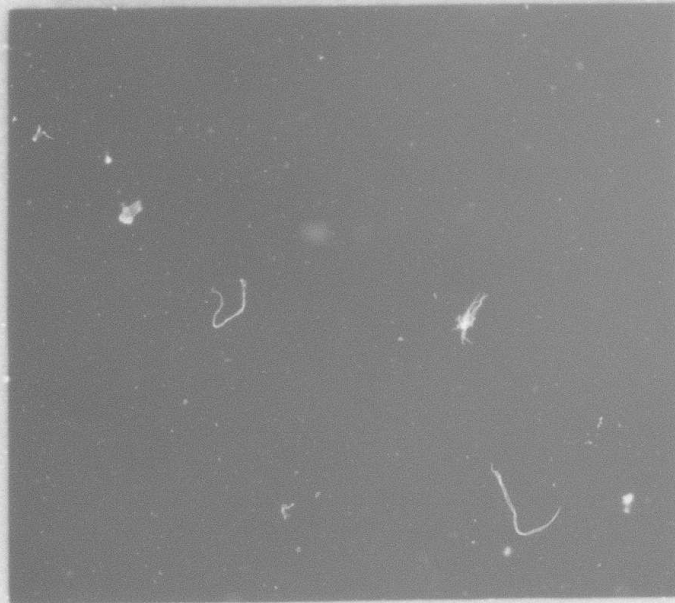
Scanning Electron Microscopy

Much of the effort during this research period was devoted to intensive study of initiation on three metals, aluminum 2024, tungsten, and lead. Although the spectroscopy covered all of the metals of interest, tungsten and lead were of particular interest because of widely varying properties which might play a role in LSD-wave-initiation processes. Table 1 presents handbook values for these properties for elemental metals of interest. Tungsten was selected in an attempt to verify prompt LSD initiation under conditions where vaporization was unlikely. Lead was chosen to enhance vaporization; however, as can be seen in the table, thermionic emission is also enhanced in this case. Additional metallic studies will be performed in the latter part of the contract to induce a vapor-dominated initiation.

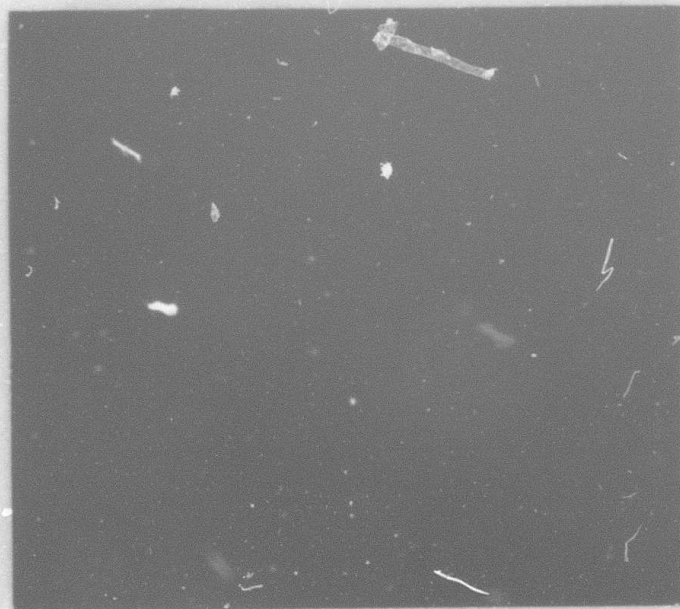
TABLE 1. HANDBOOK METAL PROPERTY DATA

Metal	Work Function, ϕ (eV)	Melting Temperature, T_m (C)	Vaporization Temperature, T_v (C)	First Ionization Potential, I(eV)
Al	3.7-4.36	660	2520	5.99
Cd	4.0-4.22	320	767	8.99
Cu	4.4-4.6	1083	2566	7.73
Mg	3.66	650	1090	7.65
Mo	4.2-4.4	2617	4607	7.10
Tl	4.0-4.45	1670	3289	6.82
W	4.5	3380	5555	7.98
Zn	4.2	420	911	9.39
Pb	3.49-3.83	327	1750	7.42

From previous work with practical aluminum 2024 surfaces, small surface features were found to be sites of plasma initiation. To provide some characterization of the lead and tungsten surfaces, additional scanning electron microscope (SEM) examinations were performed. Selected areas of aluminum 2024, tungsten, and lead samples were recorded before and after irradiation with one pulse at atmospheric pressure. The aluminum 2024 and lead samples were exposed to a peak power density of 2.14×10^8 watt/cm², while the tungsten sample was exposed to 3.2×10^8 watt/cm². These intensities were well above LSD-wave threshold as observed photographically. Representative SEM records are presented in Figure 3. Figure 3(a) and (b) illustrate typical before and after views of an aluminum 2024 surface that has initiated an LSD wave. Evidence of lamination heating to the melt temperature may be seen near the center of the SEM record. General appearance and frequency of various damage sites in the series of aluminum records is similar to that observed previously. Figure 3(c) and (d) show SEM records for the

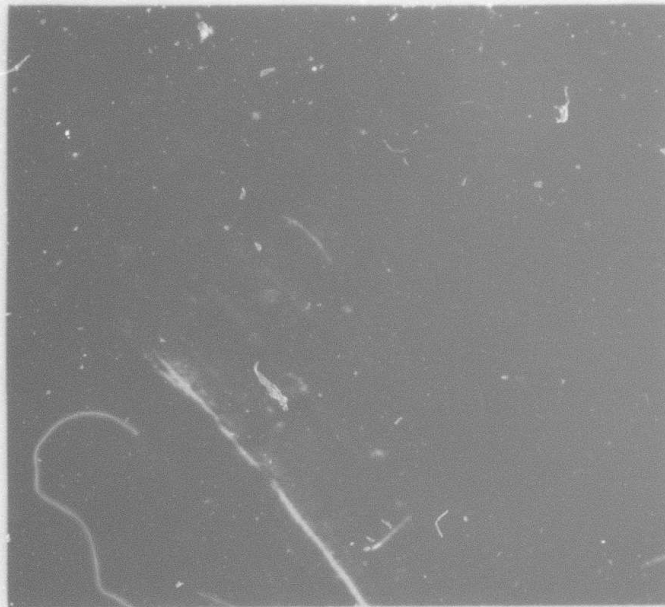


(a) Aluminum 2024 before irradiation

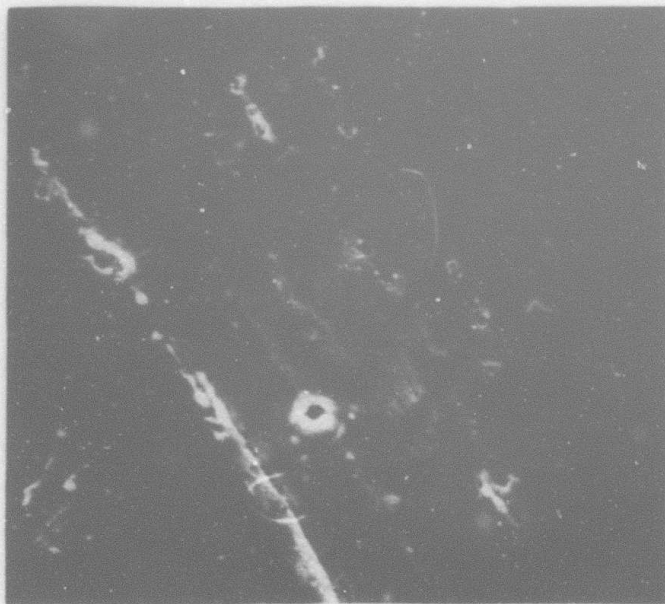


(b) Aluminum 2024 after irradiation, $G_p = 2.14 \times 10^8$ watt/cm²

FIGURE 3. SEM RECORDS BEFORE AND AFTER ONE PULSE AT ATMOSPHERIC PRESSURE (2000X)



(c) Lead before irradiation

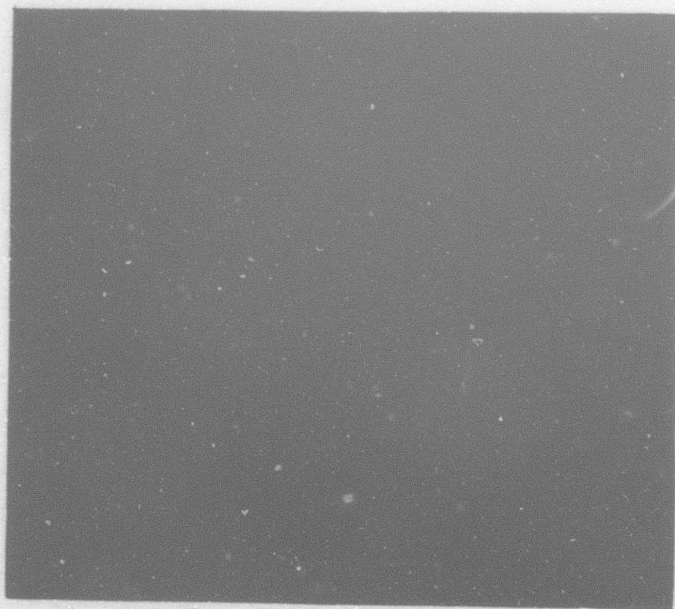


(d) Lead after irradiation, $G_p = 2.14 \times 10^8$ watt/cm²

FIGURE 3. (Continued)



(e) Tungsten before irradiation



(f) Tungsten (typical) after irradiation, $G_p = 3.2 \times 10^8$ watt/cm²

FIGURE 3. (Continued)

lead surface. Some areas showed extensive bulk surface rippling and melt while others showed mostly defect-oriented damage as shown in the figure. Clearly evident are ridge, covered pit, and covered groove defect heating regions. Preservation of certain defect details on a surface with such a low melt temperature is indicative of prompt initiation of a protective LSD wave. SEM results for tungsten are illustrated in Figure 3(e) and (f) which show records at different but typical areas on the surface (absence of distinguishing features on the relatively smooth tungsten surface made relocation of the original area difficult). No positive indication of melt was found in any of the postirradiation examinations of tungsten although the sample did cause a prompt (less than 100 nsec) initiation of an LSD wave. Surface features are evident in the SEM records, but without observed damage, the extent of local heating and the LSD initiation site density cannot be estimated.

Target Electron Emission Measurement

Atmospheric Pressure Experiments

Using the target voltage technique which was developed earlier⁽¹⁾, electron emission currents were measured for Al 2024, tungsten, and lead targets at atmospheric air pressure with various CO₂ laser irradiances. Aluminum 2024 target voltage was also studied as a function of air pressure down to 10⁻⁶ torr. The experimental arrangement was identical to that shown in Figure 12 of Reference (1) (or the arrangement of Figure 1 of this report with the electrostatic probe removed) and consisted of a target mounted on an aluminum or brass table which is connected to a standard 50-Ω coax cable through a 50-Ω terminator. The coax cable was fed directly to an oscilloscope where it was terminated with 50 Ω. The shield structure around the target was grounded through the cable shield.

Some reinterpretation of the target voltage trace was required as a result of more detailed study of the effect of target plane relative to the shield surface. The effect of target plane location is illustrated in Figure 4 which shows target voltage for three shots on the same target (brass) at 2.14×10^8 watt/cm² with the target plane at three different levels relative to the shield surface parallel to the target plane. As can be seen, the earlier part of the signal is independent of target plane position and is believed to result from thermionic emission of electrons into the un-ionized air prior to LSD-wave plasma initiation. After plasma initiation, the intense ultraviolet radiation photoionizes the air surrounding the plasma and currents are driven by the space charge field of electrons deposited in the air by thermionic emission and surface photoemission. The latter process probably dominates electron emission after plasma initiation. As can be seen in the figure, the geometry of the current flow affects the target voltage. For a target 1 mm above the shield, a conduction path to the shield is not immediately available and the measured current drops as presumably charge flowing back to the target offsets some of the photocurrent. For a recessed target, there is a conducting path to the shield and net target emission increases at the time of plasma initiation. This effect was alluded to previously, however; a more definitive breakdown time appears to be indicated in the present work. Since the change in target voltage slope is greatest for a target plane above the shield surface, this geometry was used in all of the experiments discussed below.

Standard-sized targets of aluminum 2024, lead, and tungsten were prepared and mounted on target holders as shown in Figure 1. The aluminum targets were irradiated at atmospheric pressure with peak power density in the range $0.5-5 \times 10^8$ watt/cm². A fresh target was used at each intensity level and target voltage records were obtained for several shots on the same target. A typical voltage record at 3.2×10^8 watt/cm² for aluminum 2024 is shown in Figure 5(a). A photon drag detector was

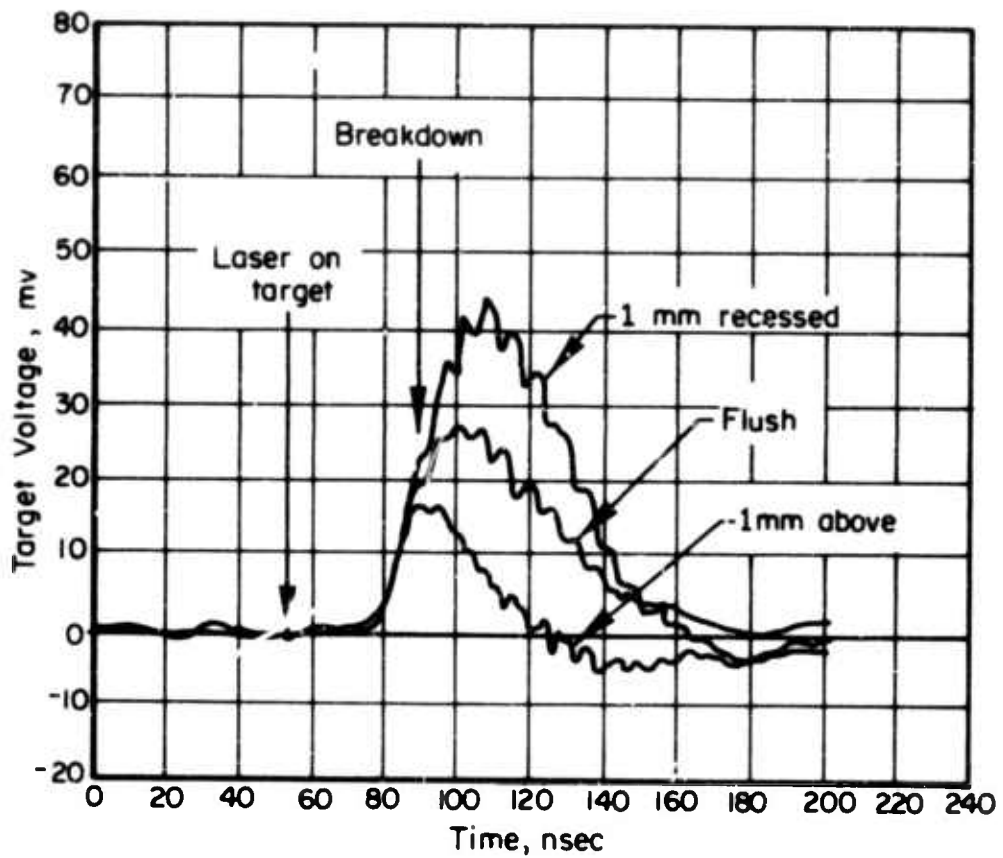
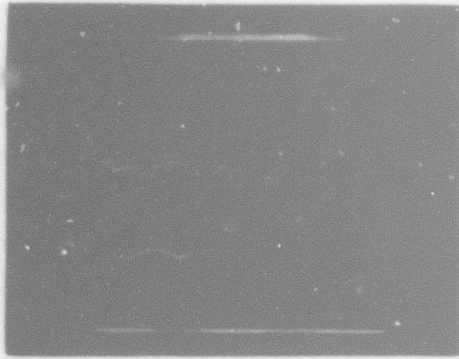
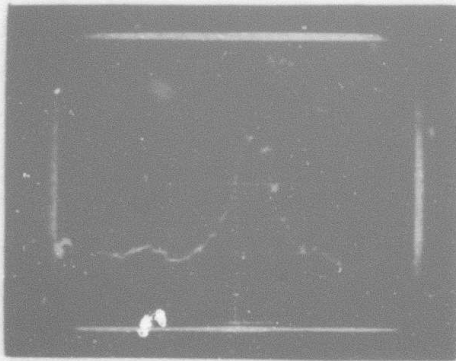


FIGURE 4. VARIATION IN TARGET EMISSION RECORDS WITH TARGET PLANE LOCATION, $G_p = 2.14 \times 10^8$ WATT/CM²



(a) Aluminum 2024 (10 mv/cm, 20 nsec/cm)



(b) Tungsten (5 mv/cm, 20 nsec/cm)

FIGURE 5. TARGET EMISSION RECORDS AT ATMOSPHERIC PRESSURE,
 $G_p = 3.2 \times 10^8$ watt/cm²

used to trigger the oscilloscope and a time calibration trace of the photon drag signal is recorded for each laser intensity level. Using this technique error in event timing is believed to be less than 4 nsec. The time that radiation first reaches the target is defined by extrapolation of the linear rise portion of the photon drag detector signal to zero intensity and subtracting 10 nsec from the time so defined. This start time occurs at 55 nsec in the records of Figure 5. For the aluminum 2024 record of Figure 5(a), emission current rises sharply beginning at about 17 nsec into the laser pulse and levels off sharply at 30 nsec, the assumed point of initiation. Very little effect of multiple shots on the same surface was observed, as expected for atmospheric pressure irradiations of metallics.

Lead and tungsten targets were also exposed to the same irradiation conditions. Breakdown times and emitted currents for lead were similar to those for aluminum 2024, while tungsten exhibited marked differences in behavior. A typical trace for tungsten at 3.2×10^8 watt/cm² is shown in Figure 5(b). The current begins to rise about 21 nsec into the pulse and breaks over at about 50 nsec into the pulse. Breakdown times for all of the irradiations are presented in Figure 6 along with a line indicating time required to deliver a constant energy density. The aluminum 2024 results agree quite well with those presented previously based on electrostatic probe measurements. Breakdown times for lead agreed fairly well with those for aluminum 2024 over the range of intensities studied. The low work function for lead may well account for the prompt initiation. Tungsten, however, exhibited considerable delay in initiation relative to aluminum 2024 and lead, which might be attributed to a relatively high work function. The delay might also be a result of a lower initiation site density.

From photographs taken during the target emission experiments the threshold for strong LSD-wave initiation was between 1 and 2×10^8 watt/cm² while plasma threshold was less than 0.5×10^8 watt/cm². The lead and aluminum 2024 LSD-wave thresholds were near 0.5×10^8 watt/cm². These

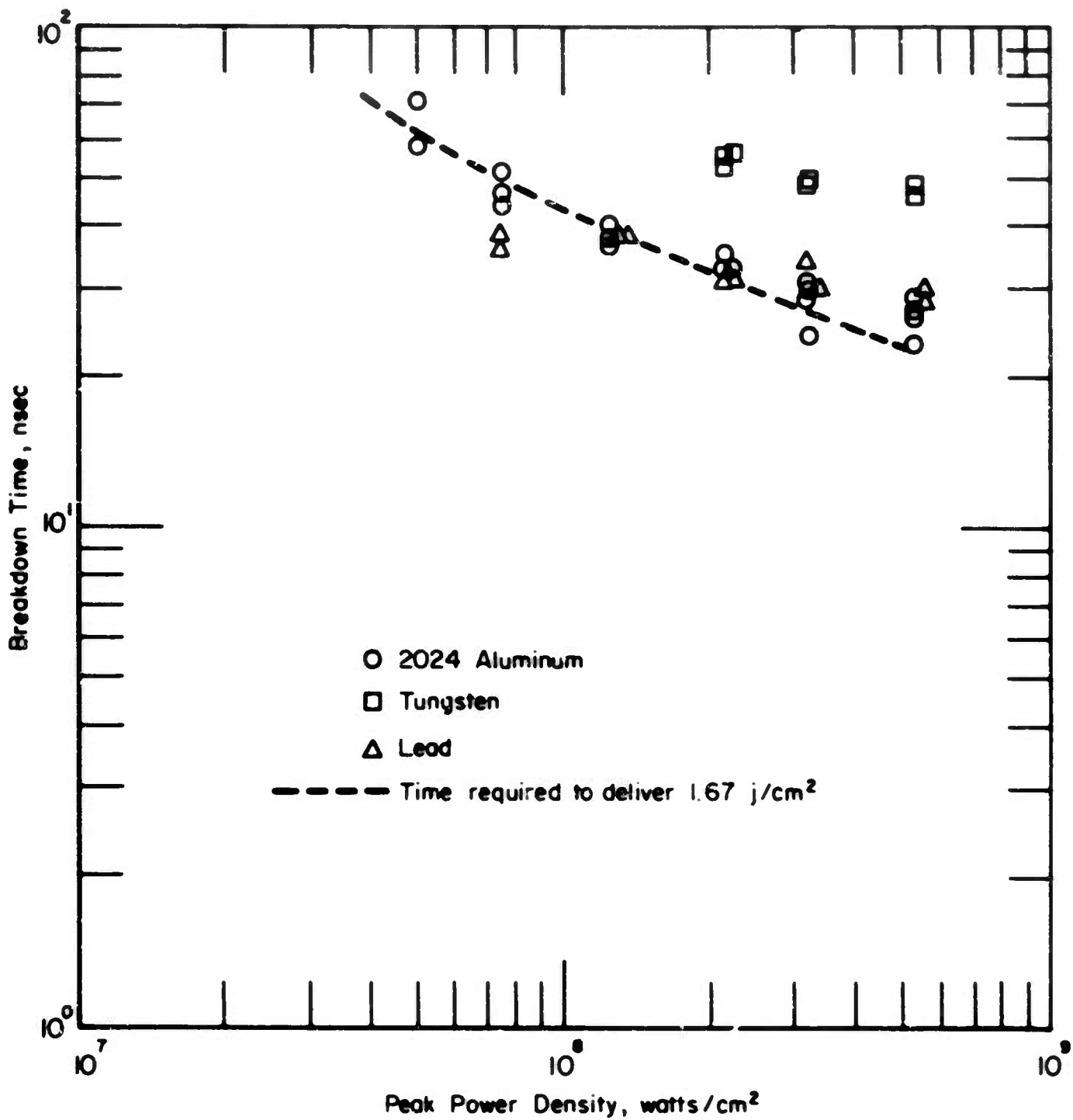


FIGURE 6. BREAKDOWN TIMES INFERRED FROM TARGET EMISSION RECORDS AT ATMOSPHERIC PRESSURE

thresholds are consistent on a relative scale with threshold data given by Hall⁽³⁾ for the same materials. The higher threshold for tungsten is particularly evident in Figure 7 which shows a measure of emission current just prior to breakdown as determined by the method discussed above. The dependence of emission current on radiation intensity is not yet understood but it is of interest to note that the emission current is about the same for the three materials at LSD-wave initiation near threshold. This might be coincidental because the local current density at initiation sites may differ significantly. The magnitude of the total net surface emission current may be estimated by the methods of Reference (1). The measured current near threshold corresponding to 4-mv target voltage was 0.16 ma. The emitted electrons diffuse to a characteristic distance from the surface given by the Debye shielding distance, h . The true surface current may be related approximately to the measured current by⁽¹⁾

$$I_{\text{surf}} = I_{\text{probe}} \frac{1}{\frac{h}{a} \left[\frac{a}{b} + \frac{3}{8} \left(\frac{a}{b} \right)^3 \right]}$$

for $h \ll a < b$, where a is spot radius and b is target radius. The Debye length is given by

$$h = 6.90 \left(\frac{T}{n_e} \right)^{1/2} \text{ cm},$$

where T is electron temperature in degrees K and n_e is electron number density in cm^{-3} . For an electron temperature of 3000 K and density of 10^{13} cm^{-3} , $h = 10^{-4} \text{ cm}$. For this case, the 4-mv target voltage would correspond to an emitted current of order 1 amp. Detailed arguments based on observed defect site density and size must be used to infer a local current density, but values of the order 10^3 amp/cm^2 do not appear unreasonable. Thomas, et al.⁽⁴⁾ have shown that the thermionic emission model is viable with one-dimensional calculations for aluminum. More refined calculations with several different materials and output relatable to experimental observables appear warranted.

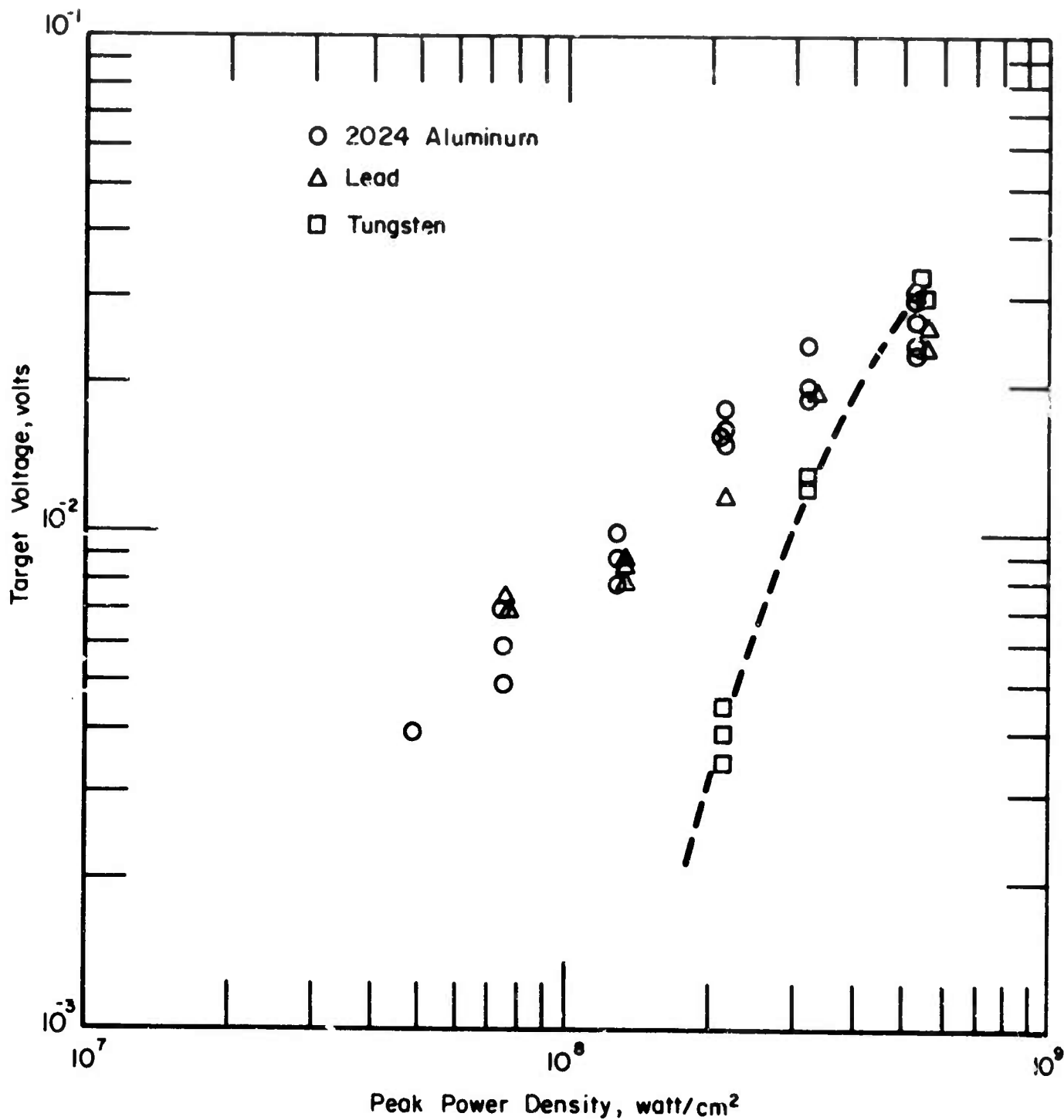


FIGURE 7. TARGET VOLTAGE AT BREAKDOWN FOR ATMOSPHERIC PRESSURE

Vacuum Experiments

Target emission measurements were also performed for aluminum 2024 samples over a range of air pressures down to 10^{-6} torr. In one series a single sample was exposed to several shots at a constant peak power density of 1.28×10^8 watt/cm² at successively lower pressures down to 10^{-2} torr. Figure 8 shows peak target voltage and target voltage at breakdown inferred by the method described above. The solid curve shows an approximately linear rise in target voltage at breakdown with decreasing pressure. At atmospheric pressure the latter voltage is also the peak voltage. Below 400 torr the peak voltage (dashed line) occurs near the laser intensity peak and is believed to result from surface photocurrents. Time-integrated photography indicated a luminous region extending back up the beam direction for all shots down to, and including, the 10 torr condition. The length of the luminous region increased with decreasing pressure as a result of higher LSD-wave speeds. Definitive breakdown times were apparent in the target voltage records only for pressures greater than 50 torr. For this pressure range, there was a finite, but small, decrease in breakdown time with increasing pressure as indicated in the figure.

The approximately linear increase in target voltage with decreasing pressure is not explainable on the basis of a simple one-dimensional model for the diffusion of emitted electrons. In this model the maximum electron density in front of the target (for constant emitted current) is related to the electron mobility, μ_e , and neutral atom density, n_n , by⁽¹⁾

$$n_e \sim \mu_e^{-2/3} \sim n_n^{2/3} .$$

Using this relationship in the Debye length formula yields the result that

$$h \sim n_n^{-1/3}$$

or $\bar{v}_{\text{probe}} \sim I_{\text{probe}} \sim n_n^{-1/3}$ for constant surface current. This is a much weaker dependence on neutral density than observed in Figure 8. In the actual

case three-dimensional electron diffusion near emitting sites may lead to much stronger dependence of the Debye length on neutral density as apparently observed.

The very steep rise in photocurrent with decreasing pressure is not easily analyzed. The change likely results from increased mean-free path of the ultraviolet radiation from the plasma which increases both the surface photocurrent and the conduction current to the shield. It is observed that the photocurrent persists at pressures below the pressure threshold for LSD wave at this irradiance condition, 10 torr. This would be expected if a plasma in the vapor occurs, as appears to be the case inferred from spectroscopic results.

Charge Collection Measurements in Vacuum Irradiations.

As discussed above, electron emission from the target surface prior to LSD-wave initiation has been observed. Since both thermionic and field emission could result in the observed currents⁽⁴⁾, electron energy measurements were performed in vacuum irradiations in an attempt to differentiate the two types of emission. A secondary result of the measurements is an estimate of the vapor plasma temperature.

Theory of the Measurement

Puell⁽⁵⁾ has derived expressions for the electron temperature, the expansion energy of the ions, and the total particle number in the plasma as a function of laser radiation intensity. The model assumes self-similar hydrodynamic expansion from a planar surface due to a continuous heating process and considers the finite focal spot size. Laser energy is deposited thermally in the electron population. In an asymptotic expansion all of the thermal energy is transformed into kinetic

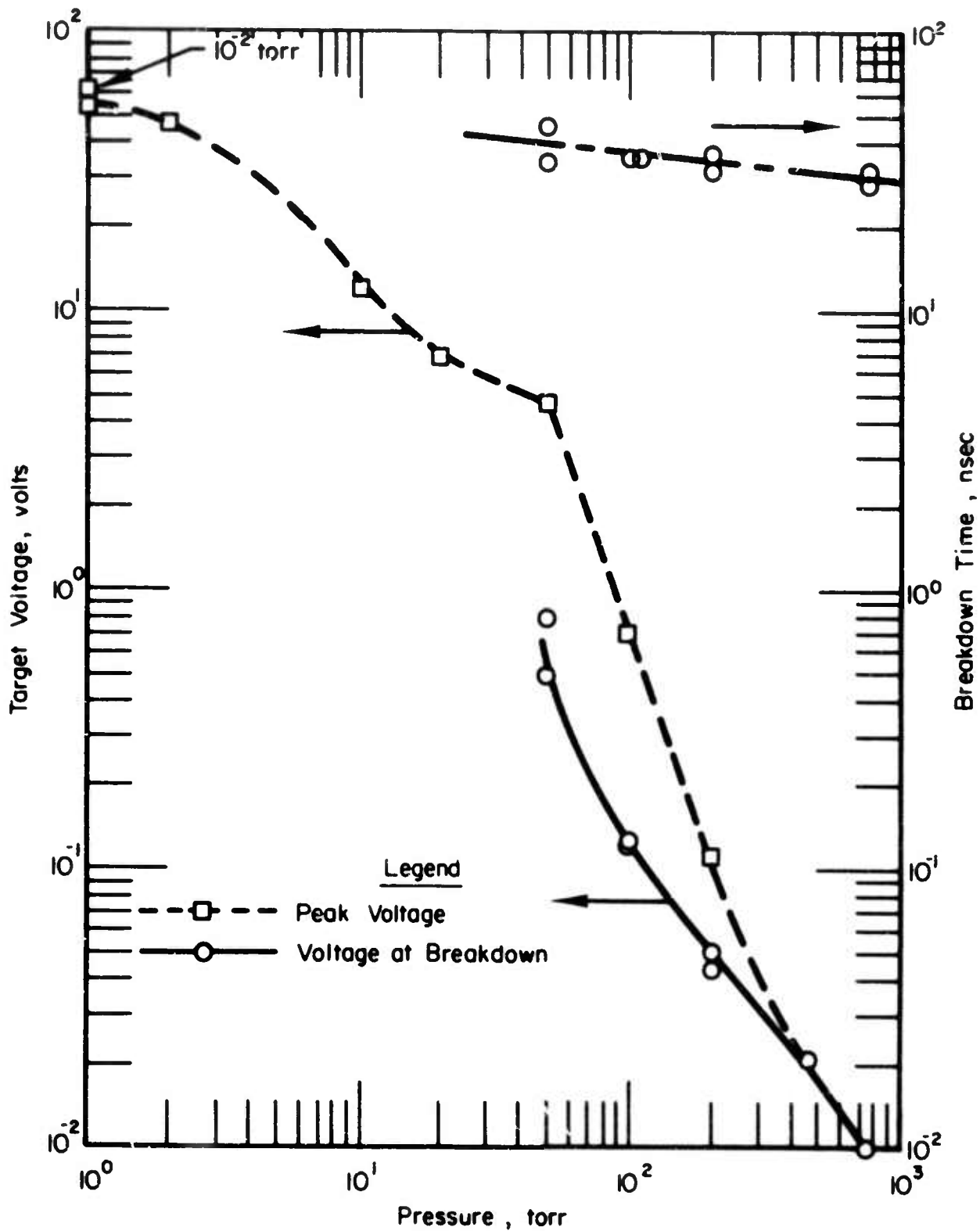


FIGURE 8. PRESSURE DEPENDENCE OF TARGET VOLTAGE AND BREAKDOWN TIME FOR ALUMINUM 2024 AT 1.28×10^8 WATT/CM²

energy (neglecting radiative effects and conduction losses). Because of charge neutrality and because of the small mass of the electrons, this energy is carried entirely by the ions. The expansion energy is found proportional to $\phi^{4/9}$, where ϕ is average power density, and assuming the plasma to be a monatomic gas, the average expansion (kinetic) energy is related to the electron temperature by

$$\bar{E}_i = 5 (\bar{Z} + 1) kT_e \quad ,$$

where \bar{Z} is the average ion charge.

This result differs slightly from the result for a free adiabatic expansion. ⁽⁶⁾ Here the asymptotic mean square ion speed is related to the acoustic velocity by

$$\overline{v_i^2} = \frac{\gamma + 1}{\gamma - 1} c_s^2 \quad ,$$

where the acoustic velocity is

$$c_s^2 = \gamma \frac{(\bar{Z} + 1) kT_e}{m_i} \quad ,$$

γ is the ratio of specific heats, and m_i is the ion mass. Hence, for a monatomic gas ($\gamma = \frac{5}{3}$),

$$\bar{E}_i = \frac{1}{2} m_i \overline{v_i^2} = \frac{10}{3} (\bar{Z} + 1) kT_e \quad .$$

Fast electrons, if obeying a Maxwell-Boltzmann distribution, would have a normalized speed distribution given by

$$N(v) = 4\pi \left(\frac{m_e}{2\pi kT_e} \right)^{3/2} v^2 e^{-m_e v^2 / 2 kT_e} \quad ,$$

where the speed v is in cm/sec and m_e is the electron mass in gm. The most probable speed of an electron is

$$v_0 = \left(\frac{2 kT_e}{m_e} \right)^{1/2} \quad ,$$

having a corresponding energy $E_e = \frac{1}{2} m_e v_o^2 = kT_e$. Since the average electron energy is

$$\bar{E}_e = \frac{3}{2} kT_e,$$

then the most probable speed is related by

$$\bar{E}_e = \frac{v_o^2}{2.35 \times 10^{15}},$$

where \bar{E}_e is in eV and v_o is in cm/sec.

Experimental Arrangement

Charge collection measurements were performed using a modified Faraday cup probe. The target-to-probe distance was usually 25 cm, and the probe was oriented $22\ 1/2^\circ$ from the target normal. Since the laser beam was incident at $22\ 1/2^\circ$ to the other side of the target normal, the angle between the laser beam axis and charge collection probe was 45° . The probe consists of a plate collector, biased to either + or - 25 volts, surrounded by a grounded housing tube. The entrance aperture is 0.56 cm in diameter, and a perforated stainless steel grid (also at ground potential) is located 0.25 cm in front of the plate. The grid transmission is $\approx 40\%$. The plate is biased through a 2-M Ω resistor, and the output is coupled through a 0.1- μ f capacitor. A termination resistance of 50 Ω was used at the input to the TEK 551 dual-beam oscilloscope. Both beams were employed in the measurements. One trace was set at a normal sensitivity depending on the peak signal, while the other trace was set five times as sensitive in order to resolve any precursor signal prior to the arrival of the plasma at the probe. An equivalent AC circuit analysis⁽⁷⁾ of the probe shows that negligible integration of the signal occurs.

When the probe is negatively biased, the velocities of the ions are determined by time-of-flight measurements over the target-to-probe distance d . The average kinetic energy is given by

$$\bar{E}_1 = \frac{1}{2} m_1 \overline{v_1^2} = \frac{1}{2} m_1 d^2 \frac{\int i(t) t^{-2} dt}{\int i(t) dt},$$

where $i(t)$ is the charge collector current. The electron energies, however, are based on a speed corresponding to the peak in the probe current with positive bias.

Experimental Results

The probe signal, whether positively or negatively biased, usually consisted of three easily identifiable components under vacuum conditions: a prompt signal, a precursor or fast-plasma component, and the normal (slower) plasma component. The precursor component was always much weaker than the normal component, and was not detectable at low intensities for several targets. For negative bias conditions, all three components gave positive-going signals corresponding to ion collection in the case of the precursor and normal plasma components, and UV-induced electron photoemission in the case of the prompt component. For positive bias conditions, all three components gave negative-going signals corresponding to fast electron arrival in the case of the prompt signal, and plasma arrival (electron collection) in the case of the precursor and normal components. As discussed below, there is evidence that the earliest signal of the fast-electron component may be due to UV radiation from the plasma striking the probe.

Shot-to-shot reproducibility of data for some of the experiments was poor. The response was a strong function of target history and depended on the number and intensity of previous shots as well as the atmosphere in which the shots were taken. In general, the average ion kinetic energy on the first shots was considerably higher than predicted for these laser intensities; however, the value of \bar{E}_1 was found to asymptotically approach some lower value after numerous shots at a particular energy. Similarly, the precursor component slowed and became less prominent. The UV-induced probe photoemission peak showed little change after multiple shots at a given

energy. The fast-electron component (positive bias) showed dramatic changes after each shot. The peak and half width of the signal decrease rapidly with multiple shots. After a few shots, the signal resembles an inverted photoemission signal of short duration. Experiments are planned which would divert charged particles away from the probe either electrostatically or magnetically to investigate the probe response to UV radiation from the laser-produced plasma with both positive and negative bias.

Multiple shots were taken on aluminum 2024 and tungsten at two intensities to assess the shot-to-shot change in prompt emission for positive bias. The most probable velocity v_0 was related to the electron energy as described above, and these data are given in Table 2. If the signal is composed of both a photoemission-related component and a fast-electron component, then as the fast-electron signal diminishes the most probable velocity and hence the electron energy would appear abnormally high. The lower energies appear more representative of the actual energies.

Table 3 presents a comparison of prompt signals obtained for both positive and negative bias. Lead was not irradiated at this high intensity. These data represent averages of several shots on the same target. The large signal observed with Zn is consistent with the strong bremsstrahlung emission for Al observed spectroscopically.

Table 4 gives the average ion expansion energies for several target materials. As discussed previously, the value of \bar{E}_1 is abnormally high for the first shot. Due to the large irradiation area, absorbed gases, surface contaminants, and/or oxide layers (all containing light elements) can lead to the calculation of an anomalously high expansion energy. If the expansion energies are related to the characteristic electron temperature of the plasmas by the model discussed above, then typically $10 \text{ eV} \leq T_e \leq 50 \text{ eV}$.

Data for shots in partial pressures of dry air (typically 0.1-20 torr) have not been analyzed pending evaluation of probe response in the absence of charged-particle impingement.

TABLE 2. ANALYSIS OF THE EFFECTS OF MULTIPLE SHOTS ON PROMPT EMISSION
(Positive Bias Signal)

Peak Intensity, w/cm^2	Target Material	Shot No.	\bar{E}_e , eV	V_o , volts
1.28×10^8	Al (2024)	1	26	0.16
		2	300	0.10
		3	(a)	0.04
		4	(a)	0.07
2.14×10^8	Al (2024)	1	3.9	0.24
		2	8.0	0.17
		3	13.2	0.11
		4	150	0.09
1.28×10^8	W	1	(b)	0.12
		2	(b)	0.04
		3	(b)	0.02
		4	(b)	0.08
		5	(b)	0.01
		6	(b)	0.006
2.14×10^8	W	1	(b)	0.17
		2	(b)	0.14
		3	(c)	+
		4	(b)	0.07
		5	(b)	0.08
		6	(b)	0.06

- (a) Signal appears to be entirely probe photoemission related.
 (b) No definitive peak could be assigned.
 (c) Data not obtained for this shot.

TABLE 3. COMPARISON OF PROMPT SIGNALS AT
 $G_p = 2.14 \times 10^8 \text{ watt/cm}^2$

Target Material	V_0 , Volts	FWHM, μsec
<u>Photoemission Signal (Negative Bias)</u>		
Zn	7.3	1.03
Ti (6-4)	0.38	0.74
Al (2024)	0.16	0.10
Cu	0.15	0.08
C	0.07	0.90
W	0	--
<u>Fast-Electron Signal (Positive Bias)</u>		
Zn	2.2	≈ 1.00
Ti (6-4)	0.20	1.00
C	0.07	0.90
Al (2024)	0.15	0.38
Cu	0.14	0.15
W	0	--

TABLE 4. AVERAGE ION EXPANSION ENERGIES

Target Material	Peak Power Density, w/cm^2	\bar{E}_i , keV	Condition
W	3.2×10^8	4.9(2) (a)	Two previous shots @ 2.14×10^8 --no signal
Al (2024)	5.35×10^8	2.3(1)	First shot with no N_2 (b)
	3.2×10^8	0.74(3)	Several previous shots
	2.14×10^8	0.64(1)	Several previous shots
Cu	3.2×10^8	2.1(1)	Several previous shots
Zn	1.28×10^8	1.3(1)	First shot
	2.14×10^8	0.27(1)	Fourth shot
Ti (6-4)	2.14×10^8	0.30(2)	Three previous shots @ 2.14×10^8
Pb	0.49×10^8	0.26(1)	Several previous shots

(a) Number of data points which were averaged.

(b) N_2 flow to laser off; peak intensity is the same, although the characteristic N_2 de-excitation tail is absent from the laser pulse.

Spectroscopic Studies

Time-integrated spectra were recorded photographically at wavelengths ranging from about 2250 to 6500 Å for several different target materials irradiated in air at pressures ranging from hard vacuum to 1 atm using the CO₂ TEA laser. The target materials irradiated were: Al (2024), Zn, W, Pb, Cu, Ti (6-4), graphite, and type 304 stainless steel. Time-resolved spectral measurements for target species were also obtained for aluminum 2024 targets in air at pressures between 1×10^{-6} torr and 1 atm. Extensive analyses of these data have not been performed but preliminary results from the UV measurements are described in the following two sections of this report.

Time-Resolved Measurements

The transient measurements with 2024 aluminum targets were performed using a SPEX, 3/4-meter Czerny-Turner spectrometer with a EMI Type 6256 photomultiplier as a detector. Output from the detector was displayed using a Tektronix 7704 oscilloscope and was recorded photographically. Transit delay time for the photomultiplier was 55 nsec and the scope delay was 55 nsec. Specific spectral lines were monitored by setting the grating angle to pass the desired wavelength. Targets were used for multiple irradiations and were not replaced for each irradiation as was done for some of the earlier studies.

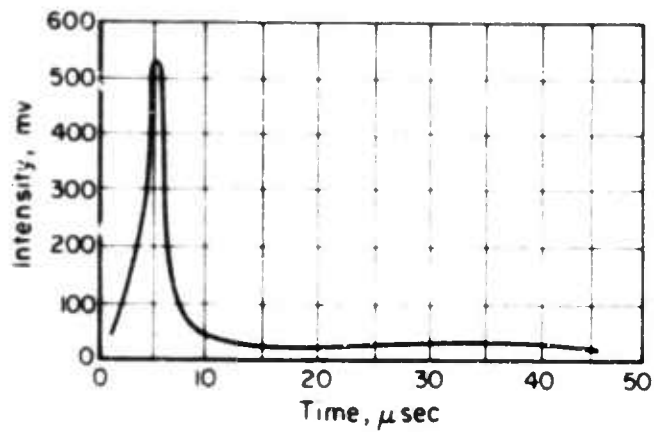
The spectral lines that were observed are listed in Table 5. The results for the Al I measurements are illustrated in Figure 9 which shows measurements made on the target surface and at a distance of 3 mm from the target. Within the limits of the variations from one irradiation to another, the three different Al I lines observed showed essentially the same transient characteristics under the same pressure and irradiance conditions. The Al I radiation shown in Figure 9(a) is typical of what would be expected for a vapor plasma expanding into a vacuum region. The sharp peak observed at 5 usec

for a 3-mm distance from the surface indicates a bulk vapor speed of 6×10^4 cm/sec which is considerably slower than the fast plasma component observed with the charge collection probe. Al I emissions associated with vacuum irradiations did not tend to persist as long as in those cases where air was present as seen in Figure 9(b). At pressures in the range of 1 torr up to 1 atm, Al I emissions persisted out to about 200 μ sec as observed in the earlier studies at atmospheric pressure.⁽²⁾ No significant differences were noted between the intensity levels at the surface and 3 mm away from the surface of the target. At early times on the surface, the photomultiplier signal for Al I (3944.01 Å) rises very sharply at approximately 60 nsec into the pulse in hard vacuum as shown by the solid line in Figure 9(c). Most of the early rise probably results from bremsstrahlung in the vapor as noted from the dashed line which shows results of a second shot with the spectrometer set about 1.2 Å off the line. Vapor is clearly evident after 300 nsec into the pulse.

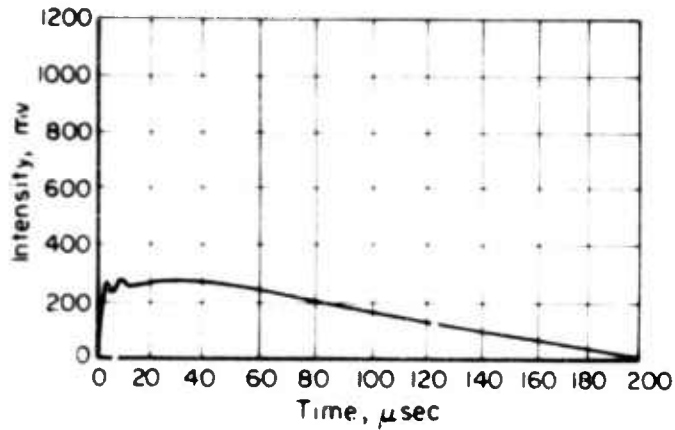
TABLE 5. EXCITED-STATE ENERGIES OF TRANSIENT SPECIES OBSERVED

Species	Emission Wavelength, Å	Energy of Excited State, eV
Al I	3050.07	7.67
Al I	3944.01	3.14
Al I	3961.52	3.14
Al II	2631.55	21.30(a)
Al II	2669.17	10.63(a)
Al II	3587.06	21.29(a)

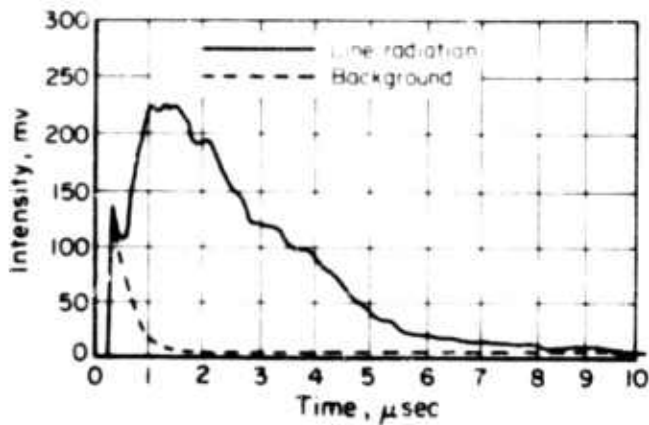
(a) Based on Al I ionization energy of 5.985 eV.



a Emission from Al I 3961.52 Å line at 3.0 mm from target surface at 4×10^{-6} torr



b Emission from Al I 3944.01 Å line at target surface at 1 torr



c Emission from Al I 3944.01 Å line at target surface at 10^{-3} torr

FIGURE 9. NEUTRAL ALUMINUM VAPOR EMISSIONS AT LOW AIR PRESSURE FOR 3.2×10^8 watt/cm².

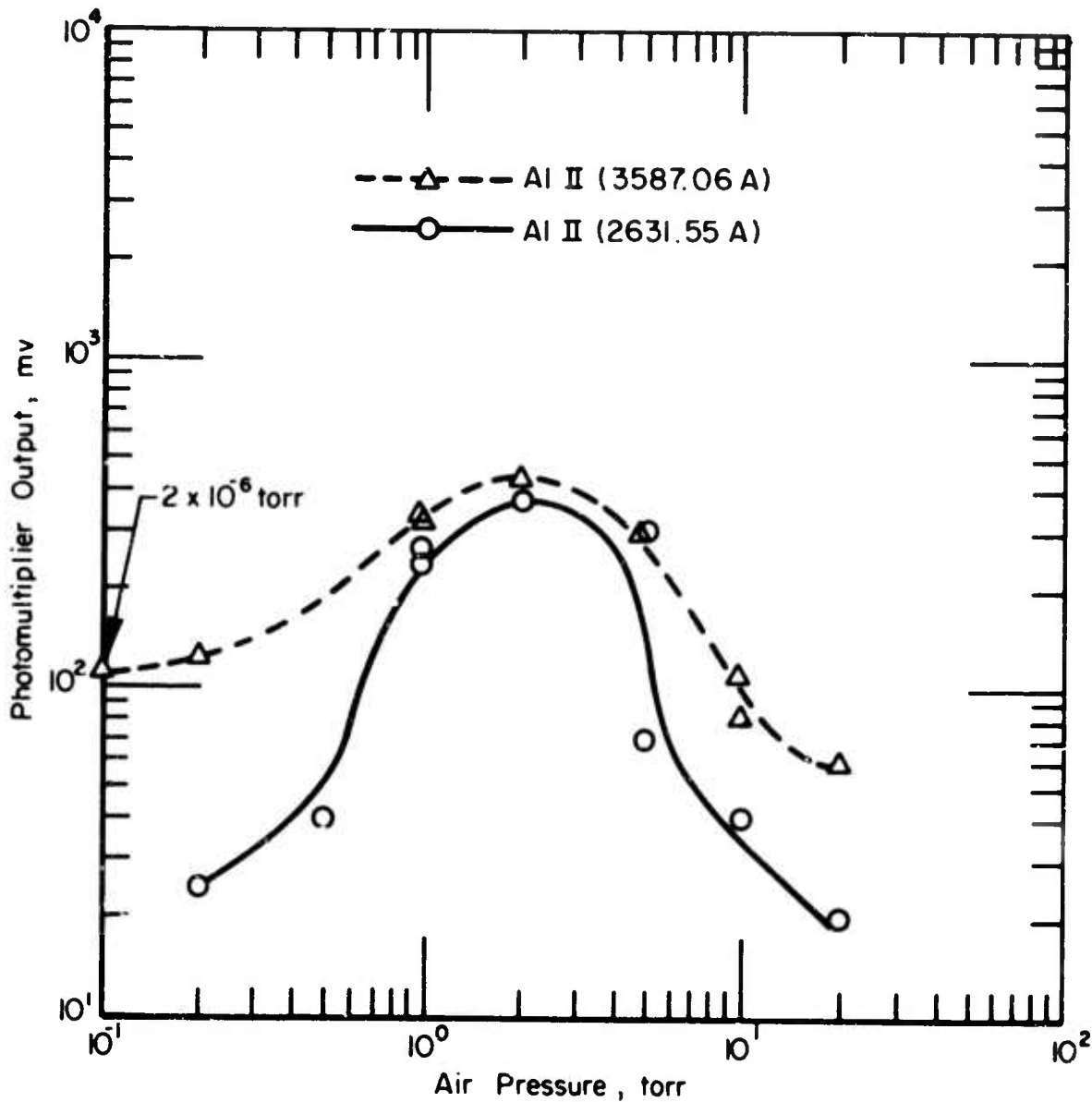


FIGURE 10. IONIZED ALUMINUM EMISSION ON THE TARGET SURFACE AT 3 μ sec ($G_D = 3.2 \times 10^6$ WATT/CM²)

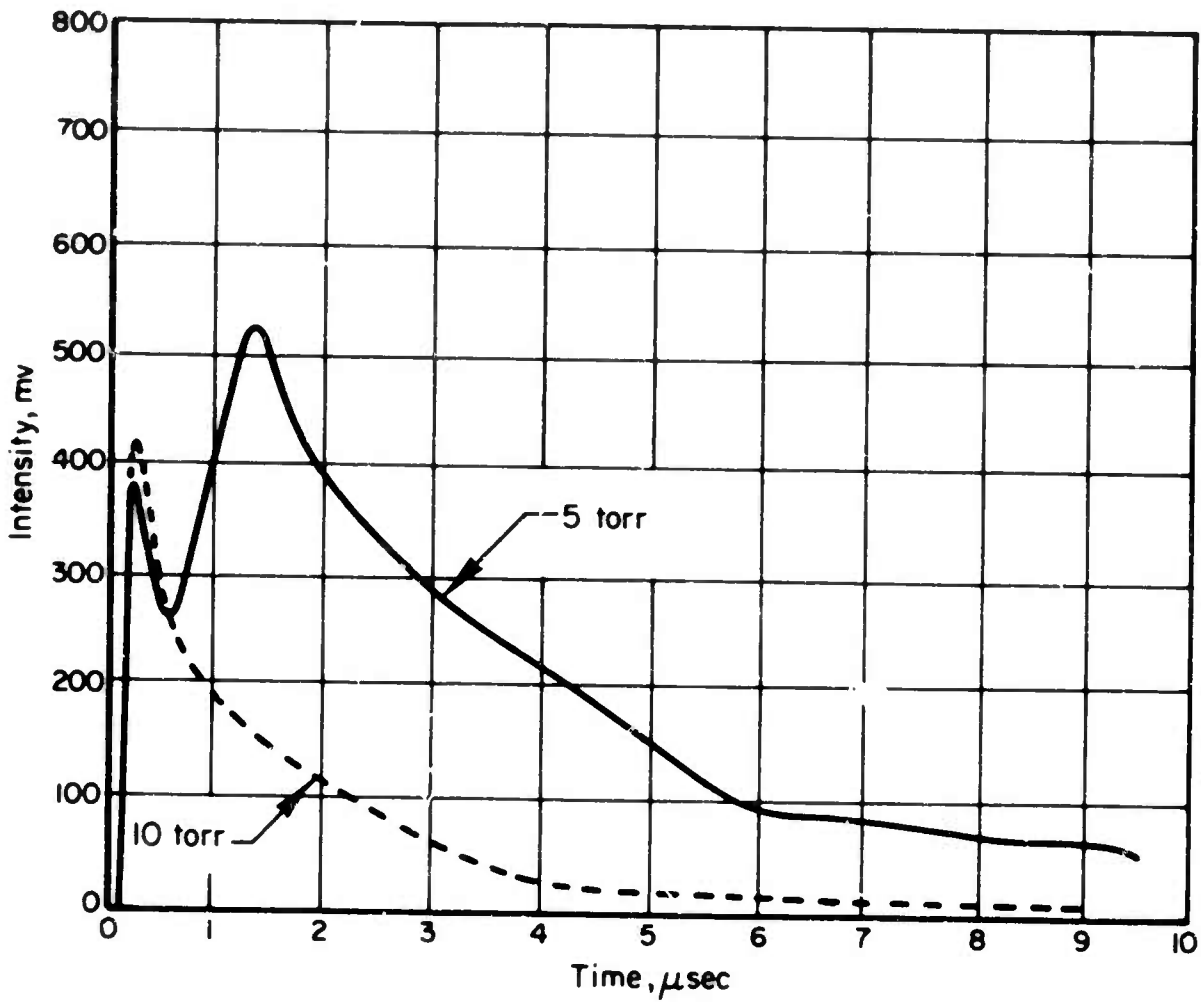
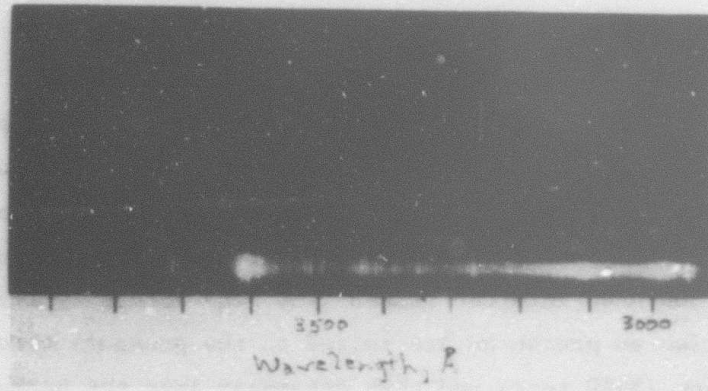


FIGURE 11. TOTAL EMISSION AT 3587.06 Å (Al II) ABOVE AND BELOW PRESSURE THRESHOLD FOR LSD-WAVE INITIATION, $G_p = 3.2 \times 10^{-2}$ WATT/CM²

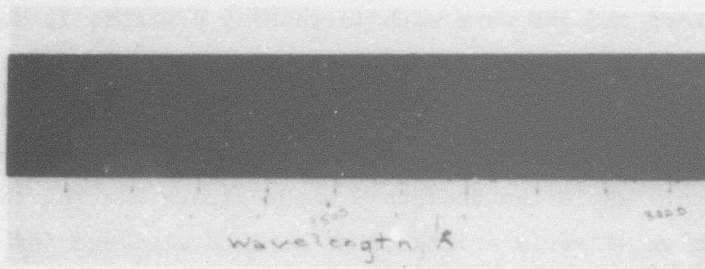
Results for the Al II ion lines were typically the same for the different wavelengths. In the range of pressures from hard vacuum to several torr, the early appearance of ionized aluminum was similar to that for neutral aluminum, i.e., the Al II emissions rise distinctly above the bremsstrahlung background about 300 nsec into the pulse. The peak intensity levels of these emissions rise as pressures are raised to the pressure threshold for LSD-wave initiation (5-10 torr) and then disappear into the background level between 20 torr and atmospheric pressure. This effect is illustrated in Figure 10 which presents the emission levels at 3587.06 and 2631.55 Å for successive shots at various pressures. Background intensity has not been subtracted from the data but only the higher pressure results are affected at 3 µsec. The onset of the LSD wave with increasing pressure is shown dramatically in Figure 11 which presents the Al II (3587.06 Å) results at pressures above and below the pressure threshold at 3.2×10^8 watt/cm². The 10-torr curve is essentially the background bremsstrahlung radiation within the precision of the measurements. While the decreased vapor plasma heating is clearly evident, the question of early existence of ionized aluminum for pressures higher than 20 torr is not resolved entirely because of the intense background radiation.

Time-Integrated Spectra

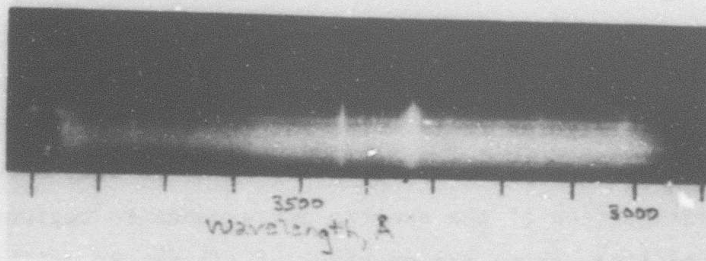
Spectra obtained with Al (2024), Zn, W, Pb, Cu, Ti (6-4) graphite and Type 304 stainless-steel targets covering the wavelength range from 2900 to 3900 Å are presented in Figures 12-19. The targets were tilted with respect to the line of sight viewed by the spectrometer so as to sample the surface emission. The lower portion of the spectra corresponds to regions near the target surface. The lines above the spectrum of (a) are Hg calibration lines. These spectra which were obtained with the targets in air at pressures of 1 atm and 1 torr, and under hard vacuum are typical of the spectra over the range from 2250 to 6500 Å. Wavelength scales shown in the figures are only approximate. In general, at 1 atm the spectra are characterized by lines



(a) 5×10^{-6} torr, 3.2×10^8 watt/cm²

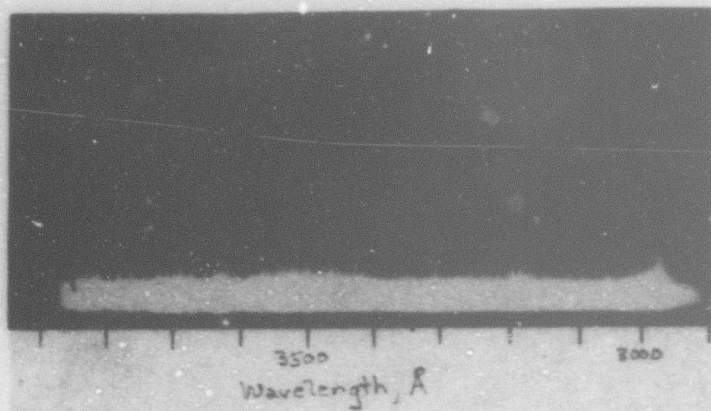


(b) 1 torr, 1.28×10^8 watt/cm²

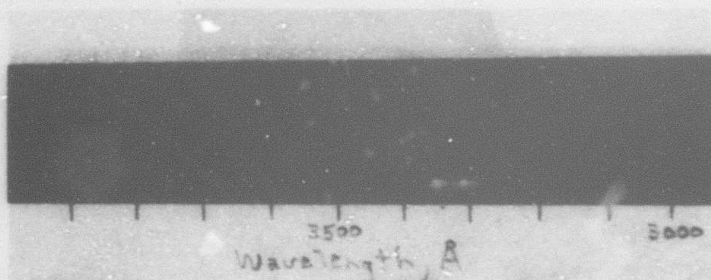


(c) 1 atm, 1.28×10^8 watt/cm²

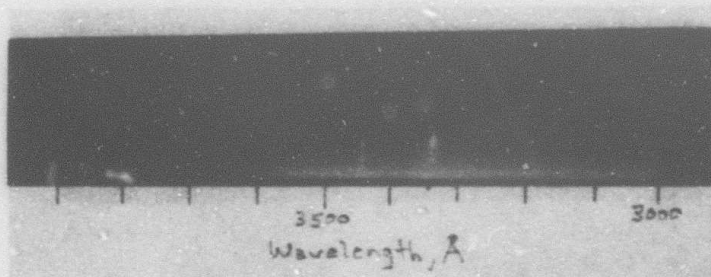
FIGURE 12. ALUMINUM TARGET SPECTRA NEAR 3500 Å



(a) 2×10^{-6} torr, 2.14×10^8 watt/cm²

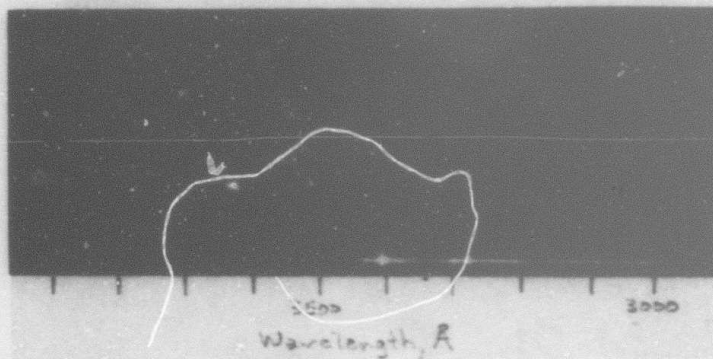


(b) 1 torr, 2.14×10^8 watt/cm²

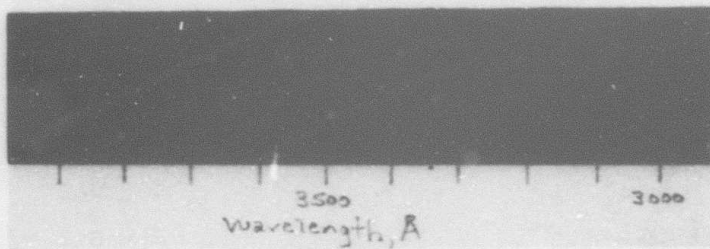


(c) 1 atm, 1.28×10^8 watt/cm²

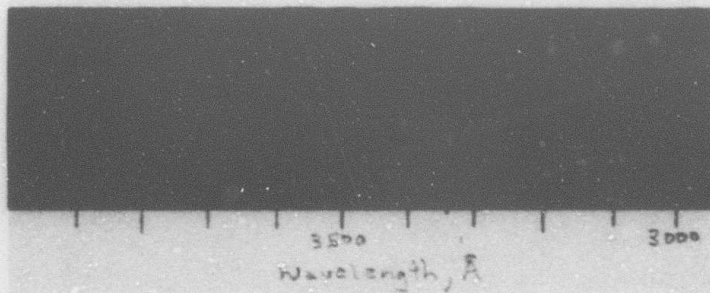
FIGURE 13. ZINC TARGET SPECTRA NEAR 3500 Å



(a) 2.5×10^{-6} torr, 5.35×10^8 watt/cm²

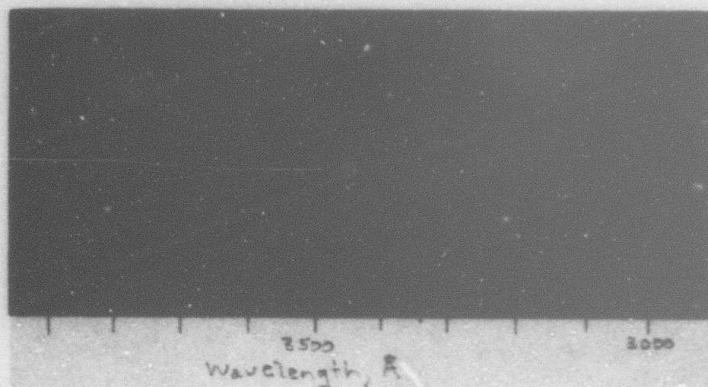


(b) 1 torr, 3.2×10^8 watt/cm²

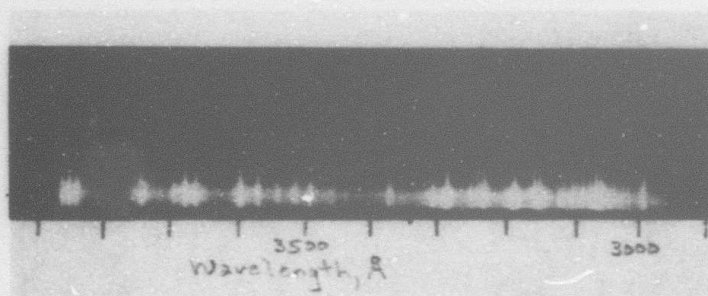


(c) 1 atm, 2.14×10^8 watt/cm²

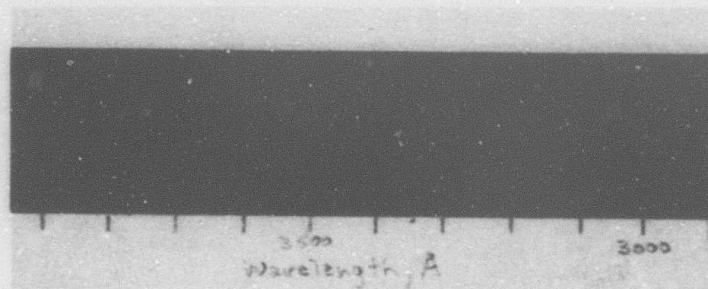
FIGURE 14. TUNGSTEN TARGET SPECTRA NEAR 3500 Å



(a) 3×10^{-6} torr, $.49 \times 10^8$ watt/cm²

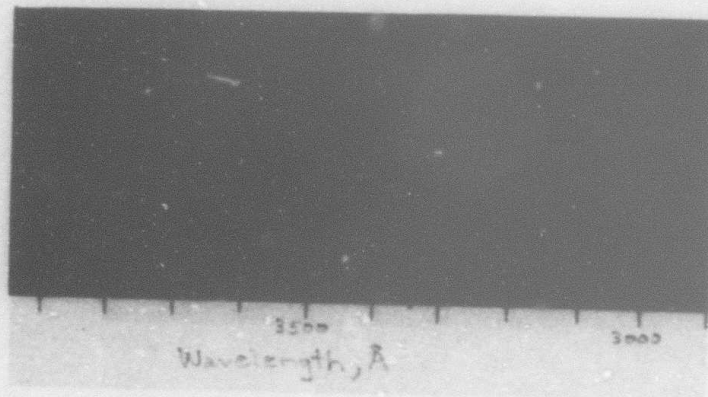


(b) 1 torr, $.75 \times 10^8$ watt/cm²

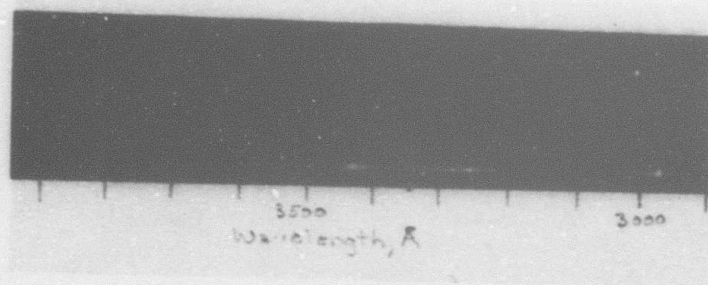


(c) 1 atm, 1.28×10^8 watt/cm²

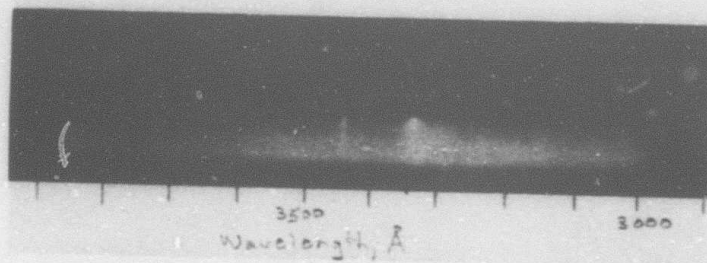
FIGURE 15. LEAD TARGET SPECTRA NEAR 3500 Å



(a) 2×10^{-6} torr, 3.2×10^8 watt/cm²

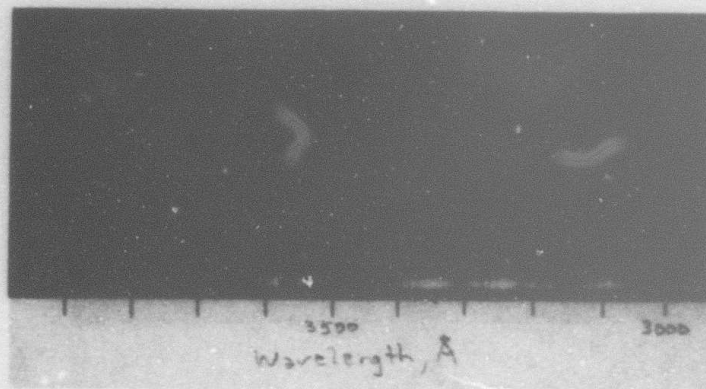


(b) 1 torr, 5.35×10^8 watt/cm²

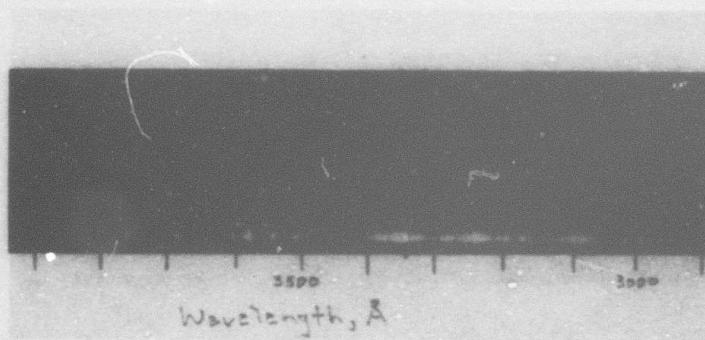


(c) 1 atm, 2.14×10^8 watt/cm²

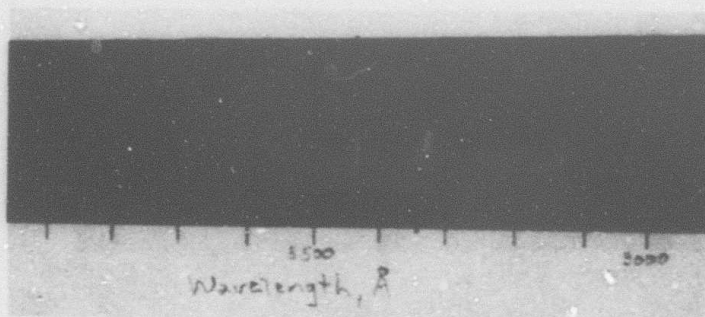
FIGURE 16. COPPER TARGET SPECTRA NEAR 3500 Å



(a) 2.5×10^{-6} torr

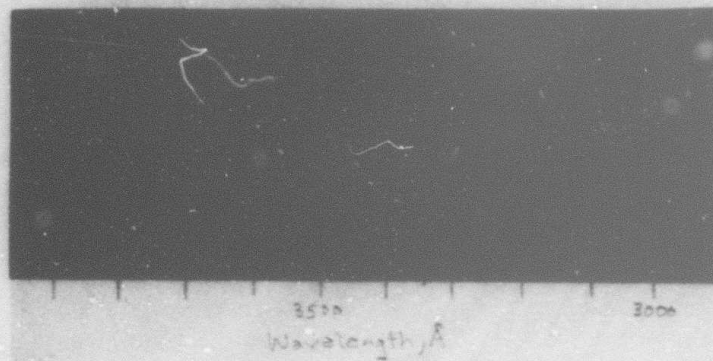


(b) 1 torr

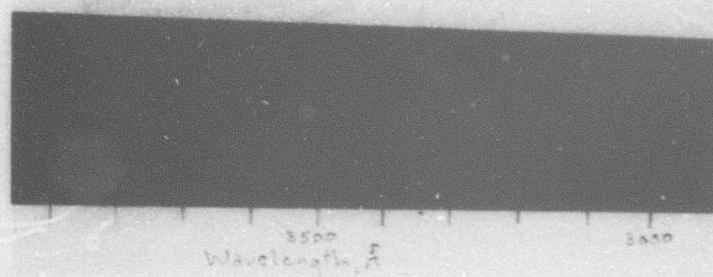


(c) 1 atm

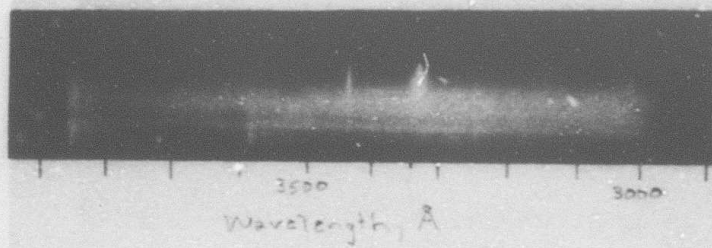
FIGURE 17. TITANIUM TARGET SPECTRA NEAR 3500 Å (2.14×10^8 watt/cm²)



(a) 2×10^{-6} torr

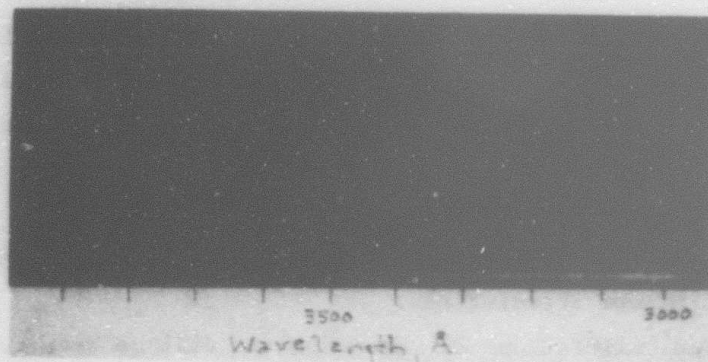


(b) 1 torr

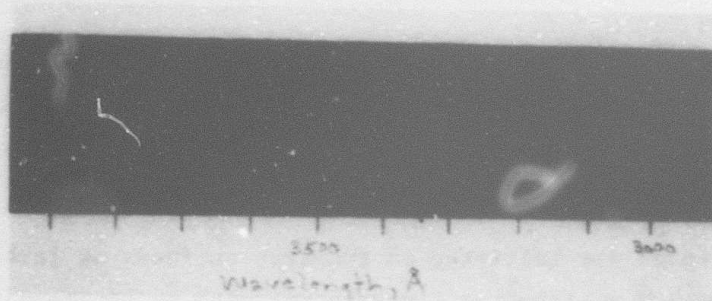


(c) 1 atm

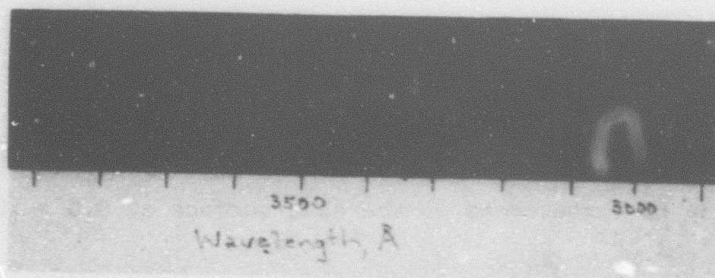
FIGURE 18. GRAPHITE TARGET SPECTRA NEAR 3500 Å (2.14×10^8 watt/cm²)



(a) 4×10^{-6} torr



(b) 1 torr



(c) 1 atm

FIGURE 19. TYPE 304 STAINLESS STEEL TARGET NEAR 3500 Å
(2.14×10^8 watt/cm²)

associated with oxygen and nitrogen from the air with some metal vapor apparently present for aluminum 2024, lead, and zinc. At the reduced pressures, however, the spectra appear to be characteristic of the different target materials. Copper which has the highest reflectivity of the materials considered here appears to produce the least target emission of the materials irradiated. Zinc, which has a low vaporization temperature, showed intense emissions in the vacuum irradiations.

Detailed calibrations of these spectra will be required for further analysis of the data.

CONCLUSIONS

Results of research on LSD-wave initiation conducted during this reporting period are consistent with the defect electron emission model for metallic initiation. Significant specific conclusions which may be drawn from the work this period are as follows.

- LSD waves are initiated on tungsten surfaces at levels above 10^8 watt/cm² at 1 atmosphere with no apparent vaporization as observed by SEM at 2000X and spectroscopy.
- Delay time to initiation for tungsten is about 20 nsec greater than that for aluminum 2024 and lead.
- LSD-wave initiation timing and target emission characteristics are similar for aluminum 2024 and lead.
- Prompt initiation (≈ 30 nsec) occurs on acrylic plastic for up to three shots on the same surface at 3.5×10^8 watt/cm².
- Measurement of the energy of electrons emitted from the target surface prior to LSD-wave initiation may be impossible because of the intense plasma-bremsstrahlung-induced, surface-photoelectron background.

- Time-resolved spectroscopy for Al II species in aluminum 2024 irradiations at different pressure levels shows decreases in peak emission intensities at the surface just above the pressure threshold for LSD-wave initiation (5-10 torr) at 3.2×10^8 watt/cm² and no detectable signal above background for pressures greater than 20 torr.
- Both neutral and ionized aluminum vapor species are detectable as early as 300 nsec for pressures less than a few torr in aluminum 2024 irradiations.

FUTURE EFFORT

During the remaining 6 months of the contract, some additional irradiations of metallic surfaces will be conducted to complete the characterization of metallic LSD-wave initiation processes. Emphasis will be placed on surface treatment and metal selection to differentiate thermionic emission and vapor breakdown mechanisms. A complete series of nonmetallic sample irradiations will also be conducted. A limited number of 1.06- μ irradiations of aluminum 2024 will be performed to assess wavelength effects. Pressure response of aluminum 2024 and acrylic plastic will be studied in air and vacuum to directly assess the effects of LSD-wave initiation.

REFERENCES

- (1) Walters, C. T., and Barnes, R. H., "An Investigation of Mechanisms of Initiation of Laser-Supported Absorption (LSA) Waves", Semi-annual Report for the period April 23-October 22, 1973, Contract No. DAAH01-73-C-0776, Battelle-Columbus Laboratories (November, 1973).
- (2) Walters, C. T., and Barnes, R. H., "An Investigation of Mechanisms of Initiation of Laser-Supported Absorption (LSA) Waves", Semi-annual Report for the period October 23, 1973-June 30, 1974, Contract No. DAAH01-73-C-0776, Battelle-Columbus Laboratories (June, 1974).
- (3) Maher, W. E., Hall, R. B., and Johnson, R. R., J. Appl. Phys. 45, 2138 (1974).
- (4) Thomas, P. D., and Musal, H. M., "A Theoretical Study of Laser-Target Interaction", Final Technical Report on Contract No. DAAH01-73-C-0930.
- (5) Puell, H., Z. Naturforsch. 25a, 1807 (1970).
- (6) Zeldovich, Ya. B., and Raizer, Yu. P., Physics of Shock Waves and High-Temperature Hydrodynamic Phenomena (Academic, New York, 1966), Vol. 1.
- (7) Beverly, R. E. III, Ph.D. Dissertation (University of Cincinnati, 1972), p 118 ff.